The Astrophysical Journal, 943:147 (12pp), 2023 February 1 https://doi.org/10.3847/1538-4357/aca89e

An Ap Star Catalog Based on LAMOST DR9

Fangfei Shi[1,2], Huawei Zhang[1,2], Jianning Fu[3,4], Donald Kurtz[5,6], and Maosheng Xiang[4,7]
[1] Department of Astronomy, School of Physics, Peking University, Beijing 100871, People's Republic of China; fangfei1420@pku.edu.cn, zhanghw@pku.edu.cn
[2] Kavli Institute for Astronomy and Astrophysics, Peking University, Beijing 100871, People's Republic of China
[3] Department of Astronomy, Beijing Normal University, Beijing 100875, People's Republic of China
[4] Institute for Frontiers in Astronomy and Astrophysics, Beijing Normal University, Beijing 102206, People's Republic of China
[5] Centre for Space Research, Physics Department, North West University, Mahikeng 2745, South Africa
[6] Jeremiah Horrocks Institute, University of Central Lancashire, Preston PR1 2HE, UK
[7] Key Laboratory of Optical Astronomy, National Astronomical Observatories, Chinese Academy of Sciences, Beijing 100101, People's Republic of China
Received 2022 November 6; revised 2022 December 1; accepted 2022 December 1; published 2023 February 3

Abstract

We present a sample of 2700 Ap stars in the Large Sky Area Multi-Object Fiber Spectroscopic Telescope (LAMOST) DR9 catalog. The candidates are first selected to be in a temperature range typical of Ap stars by using the $BP - RP$ color index from Gaia DR3. Then the 5200 Å flux depression features characteristic of Ap stars are visually checked in LAMOST DR9 spectra. The detailed spectral features are given by applying a modified spectral classification program, MKCLASS. The stellar parameters of these Ap stars, such as the $T_{\rm eff}$, $\log g$, [Fe/H], [Si/H], and $v \sin i$, are either extracted from a hot star catalog or derived through empirical relations and then a statistical analysis is carried out. The evolutionary stages are also discussed. Finally, we discuss the rotation and pulsation features of those that have TESS or Kepler light curves. Among these Ap stars, we find seven new rotation variables, one new roAp star, and a new δ Scuti pulsation of a previously known roAp star.

Unified Astronomy Thesaurus concepts: Chemically peculiar stars (226); Ap stars (50); Chemical abundances (224); Astronomy data analysis (1858); Variable stars (1761)

Supporting material: machine-readable table

1. Introduction

Chemically peculiar (CP) stars are main-sequence stars that have peculiar surface abundances characterized by enhanced (or weakened) absorption lines (Preston 1974). Their spectral types cover the early-B to early-F types, and depending on different temperatures and other atmosphere parameters, CP stars show a wide range of anomalies. It is generally accepted that some factors, such as magnetic field or binarity (e.g., Abt & Snowden 1973; Shore & Adelman 1974; Ghazaryan & Alecian 2016), make CP stars rotate slowly, reducing turbulent mixing so that atomic diffusion can efficiently work (Michaud 1970). However, these factors and how they govern the modification of atmospheric abundances are not fully understood.

Many types of CP stars have been found. Preston (1974) first divided CP stars into four main subgroups and their characteristics have been refined by several works (e.g., Alecian 1996; Hümmerich et al. 2018). The first subgroup is CP1 stars, always with weak Ca and/or Sc together with overabundances of iron-group elements, so they are also called metallic-line stars or AmFm stars. CP2 stars are the second subgroup. Most of them show some combination of enhanced Si, Cr, Sr, Eu, and rare earth elements, and sometimes, similar enhanced metal lines like CP1 stars. CP2 stars host large field and strong magnetic fields, which are believed to cause the peculiarities, so they are also called magnetic Bp, Ap, and Fp stars (or generically Ap stars hereafter). The third subgroup is CP3 stars, also known as HgMn stars or mercury-manganese stars, since they always show enhanced Hg and/or Mn. CP4 stars are the last subgroup with weak He lines so they are called He-weak stars. Besides these four groups, λ Bootis stars (underabundances of refractory elements; Murphy & Paunzen 2017), barium stars with abnormally strong lines of ionized barium (Bidelman & Keenan 1951), and carbon stars (Bidelman 1956) have also been discovered.

The Ap stars are the focus of the present research. The prime factor governing the peculiarities of Ap stars is the strong magnetic fields they host, typically roughly dipolar with field strengths of a kilogauss, or more. This strong magnetic field suppresses convection, thus providing a stable environment for ions with many absorption features to be lifted by radiation pressure to the surface against gravity. However, some other elements, especially helium, sink deeper into the sea of hydrogen.

Several catalogs of Ap and related stars have been published. After the first catalog of 6684 Ap and Am stars (Renson et al. 1991) Renson & Manfroid (2009) collected 8205 known or suspected Ap, HgMn, and Am stars from a large amount of literature. Large spectroscopic surveys provide more opportunities for us to study the spectral features of Ap stars. Scholz et al. (2019) compiled a catalog containing 238 Ap stars by detecting magnetically split lines. In their catalog, 84 Ap stars were found by Mathys (2017) and 154 Ap stars were provided by Chojnowski et al. (2019) in the Apache Point Observatory Galactic Evolution Experiment (Majewski et al. 2017). Qin et al. (2019) compiled a catalog containing 9372 Am stars and flagged 1131 Ap candidates in the Large Sky Area Multi-Object Fiber Spectroscopic Telescope (LAMOST; Cui et al. 2012; Zhao et al. 2012) DR5, with the help of machine learning by identifying several enhanced lines. Hümmerich et al. (2020, hereafter HPB2020) built a sample consisting of 1002 mCP

(magnetic CP; most Ap and He-peculiar) stars by identifying the flux depression at 5200 Å and provided the spectral classification in the modified MKCLASS program.

In this work, we introduce the data and method we used to build the catalog in Sections 2 and 3, respectively, and then compare our sample with other literature in Section 4. The stellar parameters are derived in Section 5 and finally, we discuss the photometric features in Section 6.

2. Data

LAMOST is an optical spectral telescope located in Xinglong Station of the National Astronomical Observatory, China (Zhao et al. 2012). The telescope is designed with a 20 deg^2 field of view and up to a 4.9 m effective aperture so that it is able to obtain spectra for 4000 targets with magnitude brighter than $r = 19$ at a resolution $R \simeq 1800$ at one time in low-resolution mode (Zhao et al. 2012). Taking advantage of the instrument, the LAMOST survey was launched in 2011 aiming to collect spectra for all the objects of interest covering from $-10°$ to $+90°$ decl. This is where our spectra come from. Up to DR9, LAMOST has obtained 11,791,589 spectra with spectral resolution $R \simeq 1800$ approximately covering a wavelength range of 3700–9000 Å.

Gaia (Gaia Collaboration et al. 2016) is a space telescope launched in 2013. It observes stars in a wide G band (330–1050 nm) together with a blue band, BP (330–680 nm) and a red band, RP (640–1050 nm) down to $G \sim 20.7$ mag and also collects middle-resolution spectra for stars brighter than 16.2 mag in the G band. With the astrometric and photometric measurements, including the distance, proper motion, and magnitude of billions of stars in the Milky Way, it can be used to study not only the stellar physics but also the formation and evolution of the Galaxy. Up to Gaia DR3, the astrometric and photometric measurements for nearly 2 billion sources brighter than $G = 21$ have been released (Babusiaux et al. 2022). In this work, the parallax and the color index, $BP - RP$, are obtained from Gaia DR3.

Gaia also gives stellar astrophysical parameters in DR3 (Andrae et al. 2022; Recio-Blanco et al. 2022). These parameters are measured in two ways: one is based on astrometry, photometry, and low-resolution spectra; the other is based solely on spectra from the Radial Velocity Spectrometer, which provides middle-resolution spectra ($R \simeq 11{,}500$). These parameters are used as input to produce further results, such as mass, age, and evolutionary stage.

In order to construct a large sample of Ap star candidates, a data set of stellar spectra with high signal-to-noise ratios (S/Ns) in the Sloan g band (S/N $g \geqslant 50$) was chosen from LAMOST DR9, which includes 2,775,994 spectra. As the temperature range of Ap stars is above 6000 K, we first selected stars with B, A, and F spectral classifications given by LAMOST. Since some stars do not have accurate LAMOST stellar classifications, we also considered the color index, $BP - RP$, given by Gaia DR3. According to Mamajek (2022), $T_{\rm eff} > 6000$ K corresponds to an extinction-corrected color $(BP - RP)_0 < 0.767$. Here, the extinction was calculated through a new three-dimensional map of dust reddening, BAYESTAR (Green et al. 2019), based on Galactic longitude l, Galactic latitude b, and parallax from Gaia DR3. We select 929,043 spectra through $(BP - RP)_0$. Some stars do not have distance measurements, so it is impossible to calculate the de-reddened $(BP - RP)_0$. For these stars, we ignore the reddening. Their $(BP - RP)_0$ must be smaller after considering extinction; thus, the $T_{\rm eff}$ must be higher than 6000 K. So we also selected 2926 spectra without distance measurements but with $(BP - RP) < 0.767$. In total, 931,969 spectra pass the color criterion.

3. Catalog

3.1. Flux Depression

There is a flux depression at 5200 Å that is essentially only seen in the spectra of magnetic CP stars (Maitzen et al. 1998, 2018). This depression feature was first discovered by Kodaira (1969) together with similar flux depressions at 4100 and 6300 Å through spectrophotometric observations of the Ap star HD 221568. The combined contributions of Si, Cr, and Fe absorption at 5200 Å is the main cause of the depression (Khan & Shulyak 2007). Stigler et al. (2014) found that the three-filter Δa photometric system (Maitzen 1976) can be used to detect the peculiarity related to the 5200 Å region.

In this system, two intermediate band filters (g_1 at 5020 Å and g_2 at 5240 Å) are used along with the Strömgren y filter. The flux at g_2 is compared with that at g_1 and y. The index is introduced as

$$a = g_2 - (g_1 + y)/2,$$

and it describes the depth of the flux depression at 5200 Å. As shown in Stigler et al. (2014), the index a depends on the color index, in other words, depends on the $T_{\rm eff}$. The relationship between index a and $(B - V)_0$ color is nearly linear for bluer stars. To compare the a values of peculiar stars and non-peculiar stars, an intrinsic peculiarity index, Δa, is used:

$$\Delta a = a - a_0,$$

where a_0 is the index for non-peculiar stars with the same color. Then the peculiar stars are selected with a large enough Δa. This is the traditional way to examine this depression feature, as HPB2020 used in their work: they calculated Δa by comparing a indices with those of normal stars and selected the stars with Δa larger than +75 mmag as their mCP star sample.

In Figure 1, we plot Ap stars and normal stars in the $((BP - RP)_0, a)$ diagram with the expectation that a line can separate them, since Ap stars should have larger a compared to non-peculiar stars with the same color, $(BP - RP)_0$. To test this, we selected the mCP stars in HPB2020 and chose 1000 normal stars in LAMOST DR4 that are not in the HPB2020 samples. $(BP - RP)_0$ and a were calculated for these stars. To calculate the magnitudes in each filter, the spectra were normalized to the flux at 4030 Å and then folded with the filter curves defined in Kupka et al. (2003). The left panel in Figure 1 shows that we do find a line that separates the two groups.

There are 931,969 spectra that pass the color criterion and are also plotted in the $(BP - RP)_0$ (or $(BP - RP)$) versus a diagram (right panel in Figure 1). In the diagram, there are 10,750 spectra above the line. This indicates that these spectra have significant deep absorption around 5200 Å.

Since the depression has multiple contributions from Si, Cr, and Fe, it is more likely to be a blended absorption (red one in Figure 2) rather than lines (blue line in Figure 2). For assurance, all 10,750 spectra passing the index a criterion are inspected one by one to make sure that the selected spectra have obvious depression features and enhanced absorptions at several Si, Cr, Sr, and Eu lines. For one star, only the spectrum

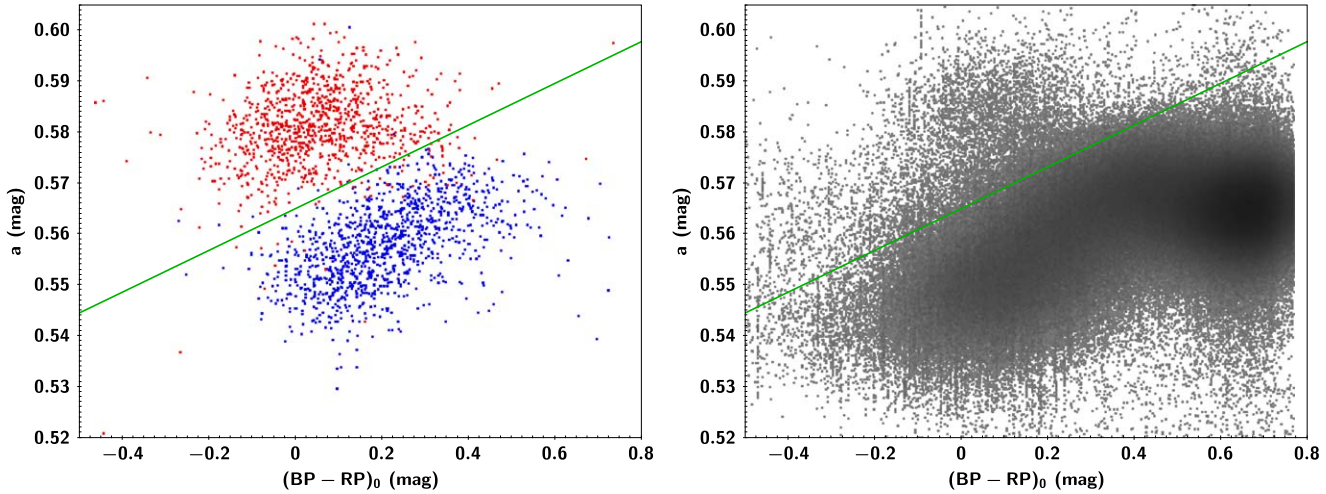

Figure 1. Left: the distribution of Ap stars (red) and non-peculiar stars (blue) on the $(BP-RP)_0$ vs. a diagram. The green line separates the two groups. Right: the distribution of the spectra selected by $(BP-RP)_0$ (or $(BP-RP)$) and $T_{\rm eff}$ in Section 2 on the $(BP-RP)_0$ (or $(BP-RP)$) vs. a diagram. The green line is the same as that above.

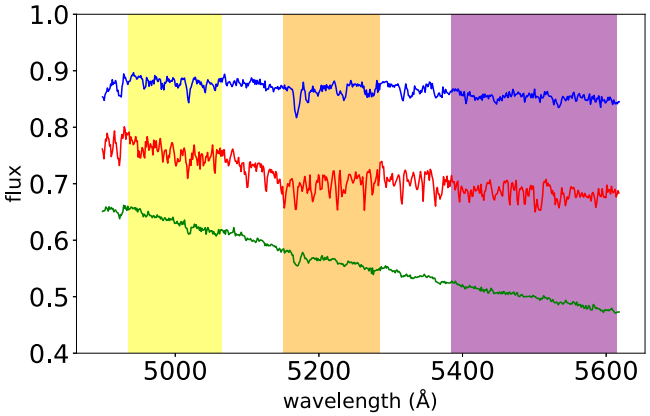

Figure 2. The 4900–5600 Å region of example spectra of an Ap star (red spectrum in middle) and a normal star (green spectrum in the bottom) with similar $T_{\rm eff}$. The blue one (top), as an example, shows the spectrum of a star whose large a index is caused by absorption lines in the g_2 band rather than a blended absorption; thus, it is removed after inspection. The main ranges of the g_1, g_2, and y filters are shaded in yellow, orange, and purple, respectively. The spectra are normalized at 4030 Å. For clarity, the continuum of the Ap stars has been offset by 0.1.

with the highest S/N was chosen. After this, we have 2700 individual Ap stars remaining.

However, the 5200 Å depression is only an indicator of enhanced Si, Cr, or Fe, and this feature in some Ap stars may not be significant enough to be selected by our criteria, so our Ap stars are biased toward those with significant flux depressions at 5200 Å. Some Ap stars with ambiguous depression features may also be missed in this process since we want to ensure a pure Ap star sample.

3.2. Peculiarity Features

MKCLASS is an automatic classification code designed to classify spectra following the traditional classification process done by humans (Gray & Corbally 2014). The current MKCLASS (v1.07) was developed to identify spectral features in the range of 3800–5600 Å by comparing the observed spectra with standard ones in a specific library. The spectra in different libraries were obtained with different resolutions and wavelength ranges. MKCLASS is able to give not only the spectral and luminosity classification but also a few sets of spectral peculiarities, so that it can help search for CP stars. For example, Gray et al. (2016) applied the MKCLASS to classify the spectra in the LAMOST-Kepler project and found 1067 Am stars in 3088 A4 to F1 dwarfs and subgiants. Currently, the lines related to Ap stars that MKCLASS can identify are the blend contributions from Si II, Sr II, and Cr II at 4077 Å, the blend of Si II and Eu II at 4130 Å, and the Eu II 4205 Å line.

Considering the special features of Ap stars, we modified the MKCLASS code following the methods developed by HPB2020. Apart from that, we abandon two Si II lines beyond 5600 Å and He I lines, we use the same line list, including two blend lines (4077, 4130 Å), four Si II lines (3856, 4200, 5041, 5056 Å), two Cr II lines (3866, 4172 Å), one Sr II line (4216 Å), and one Eu II line (4205 Å). The original library, libnor36, and the library built by HPB2020 with LAMOST spectra, liblamost, are used because both have similar resolution and flux processing as the spectra in LAMOST. Detailed spectral classifications are given in the catalog in the form of element+wavelength following the work of HPB2020.

The two libraries do not always assign for the same star the same spectral type. The typical uncertainty of the spectral type is a ±1 subclass, and for some stars, this increases up to ±2 subclasses. Considering that the peculiarities in Ap star spectra make the classification difficult, we use two subclasses as a criterion for the reliability of spectral classifications. If the deviation of the two spectral classifications is not larger than 2, then the classification results are considered reliable. For those that are less reliable, the classification results are flagged with star marks in Columns 8 and 9 in the catalog.

The table in the Appendix shows an extract of our catalog of the total 2700 Ap stars and is organized as follows:

1. Column 1: Observation ID in LAMOST,
2. Columns 2 and 3: R.A. and decl.,
3. Column 4: Absolute G magnitude estimated from Gaia DR3 apparent G magnitude and distance,
4. Column 5: De-reddened $(BP-RP)_0$ (or $(BP-RP)$),
5. Column 6: a index,
6. Column 7: Distance given by Bailer-Jones et al. (2021),

Table 1
Number of the Stars in Common in Each Catalog

Catalog	Numbers of Stars in Total	Numbers of Stars within the Color Range	Numbers of Stars above the Line in Figure 1	Numbers of Stars in Our Ap Catalog
Renson et al. (1991)	6684	125	59	52
Renson & Manfroid (2009)	3652	134	70	68
Scholz et al. (2019)	237	24	20	20
Qin et al. (2019) all	9372	9158	573	65
Qin et al. (2019) with Ap flag	1131	995	130	44
HPB2020	1002	996	935	927

7. Columns 8 and 9: Spectral classification using the standard star libraries liblamost and libnor36, respectively,
8. Column 10: Rotation and pulsation features,
9. Column 11: Gaia ID.

4. Comparison with Other Catalogs

There are other peculiar star catalogs in the literature. In this section, our samples are compared with these catalogs and the number of stars in common in each catalog is listed in Table 1.

Renson et al. (1991) and Renson & Manfroid (2009) published two editions of catalogs including Ap stars. The former contains 6684 Ap and Am stars while the latter contains 3652 Ap stars. After crossmatching with our work, there are only 52 and 68 stars in common, respectively. Their work was mainly for bright stars that are not the targets of LAMOST, so there are only 270 stars observed by LAMOST. About half of these stars have a large a index and passed our depression inspection. The other half of the stars are missed. As discussed in Section 3, our method based on depression features cannot perfectly select all the Ap stars.

Scholz et al. (2019) built a catalog that contains 237 Ap stars by measuring magnetic fields or resolved magnetically split lines. Since the most obvious feature that can distinguish Ap stars from other CP stars is magnetic fields, their catalog provided reliable Ap star samples. Twenty-four stars are also selected through color by us and among them, and 20 stars have large a indices and are selected as Ap stars in this work.

Qin et al. (2019) published 9372 Am stars in LAMOST DR5, and flagged 1131 Ap star candidates. Sixty-five stars are in common with our stars, and among them, 44 stars are flagged as Ap stars in their work. As discussed in HPB2020, Qin et al. (2019) tended to find CP1 (Am) stars with large differences ($\geqslant$5) between the spectral subtypes obtained from Ca lines and H lines given by MKCLASS, which is not a typical feature of Ap stars.

We also compare our sample with that of HPB2020. Both works identified Ap stars using the 5200 Å depression; thus, a large overlap between these two samples can be expected. There are 927 stars in common with their 1002 mCP stars. Four stars are missed after crossmatching with Gaia DR3 using positions within 4″; for assurance, we did not include them in our sample. Sixty-three stars do not have large enough a index and eight stars do not pass our inspection process. As shown in the left panel of Figure 1, some Ap stars are located below the criteria line, which means our catalog may have missed some Ap stars with an unconspicuous a index.

There are 1147 stars in our candidates that are present in LAMOST DR4 but were not included in 1002 mCP stars from HPB2020. To make sure these stars have peculiarities, their spectra are visually checked by comparing them with the spectra of the standard stars in the libnor36 library with similar spectral types (the spectral types are given by MKCLASS). Among these 1147 stars, 16 stars are also in Renson et al. (1991) and Renson & Manfroid (2009). It is therefore possible that HPB2020 may have missed more Ap stars. Another difference between our two methods is that when examining the 5200 Å depression HPB2020 compared this absorption feature with some standard stars while we use an empirical line on the $(BP-RP)_0$ versus a diagram. Our methods may let more stars pass the visual inspection process, so that more Ap stars are found. Among our 2700 Ap stars, 2074 stars were observed before LAMOST DR4, and account for up to 77% of the total. This is reasonable because more than 66% of the DR9 data was observed before DR4.

5. Stellar Parameters

Some statistical properties of our final Ap stars are discussed in this section. The statistical distributions of several parameters, such as the $T_{\rm eff}$, $\log g$, mass, and absolute magnitude, are shown first. Then the $v \sin i$, [Fe/H], and [Si/H] of Ap stars are compared with normal stars. Finally, the evolution stages are discussed.

5.1. T_{eff}, log g, Mass, and Absolute Magnitude

In this section, we show how to derive the stellar parameters for the Ap stars investigated in this paper and discuss the distribution of their parameters. $T_{\rm eff}$ values were extracted from Xiang et al. (2022), who provide the basic stellar parameters for 352,987 hot stars from LAMOST DR6. They developed a spectral fitting tool called The Payne to derive 11 parameters including the $T_{\rm eff}$. Using this hot star catalog, we extract $T_{\rm eff}$ values for 2550 stars in our Ap star catalog.

Panel (a) in Figure 3 shows a histogram of the $T_{\rm eff}$ of our Ap stars. The distribution has a peak of around 8000 K. None of these stars have a $T_{\rm eff}$ lower than F stars ($T_{\rm eff} < 7500$ K) or higher than B stars ($T_{\rm eff} > 30{,}000$ K).

To calculate the absolute G magnitudes, extinctions were obtained through BAYESTAR, as mentioned in Section 2, and the distances were extracted from Gaia DR3 (Bailer-Jones et al. 2021). There are two types of distances given in their work, one is the geometric distance, which is derived from parallaxes, and the other is the photogeometric distance, which additionally uses the color and apparent magnitude of a star. According to Bailer-Jones et al. (2021), although two distance measurements give similar results at a small distance, the photogeometric distances perform better at a larger distance. Therefore, the photogeometric distance is used to calculate the extinction. Panel (b) in Figure 3 shows a histogram of the absolute G magnitude of our Ap stars.

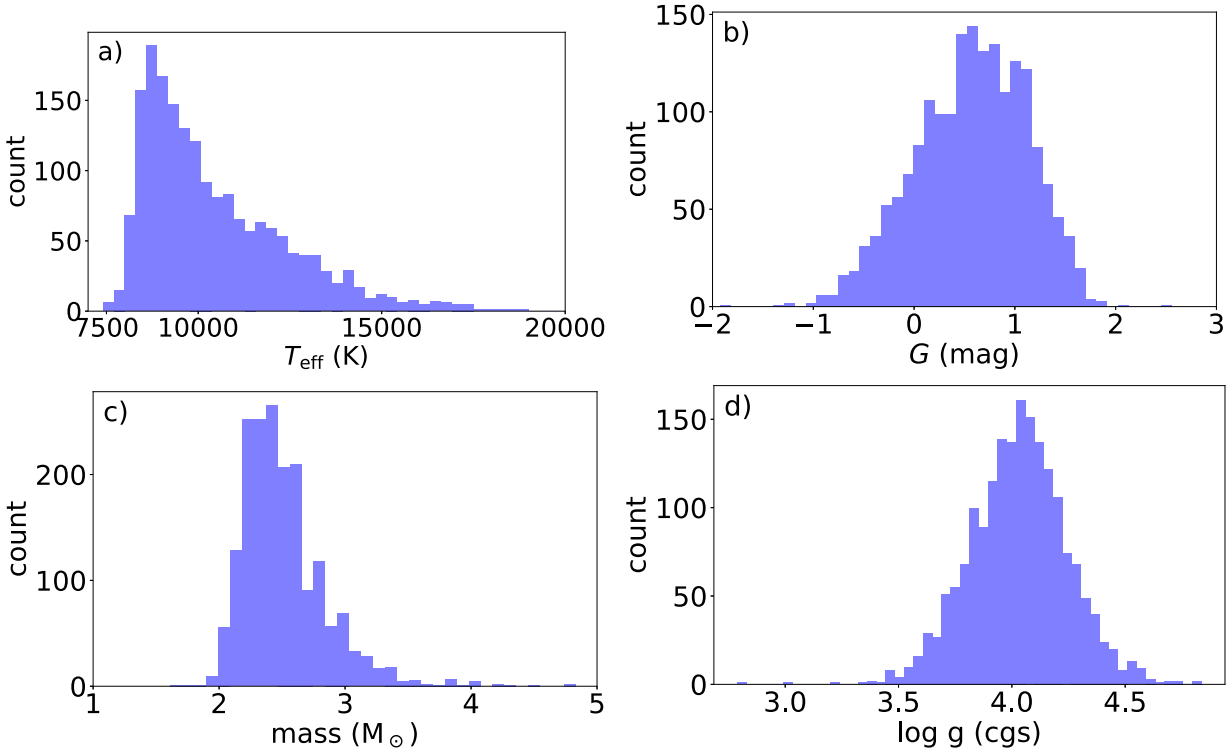

Figure 3. Histograms of the effective temperatures (a), absolute G magnitudes (b), masses (c), and $\log g$ (d) values on the main sequence of our Ap stars.

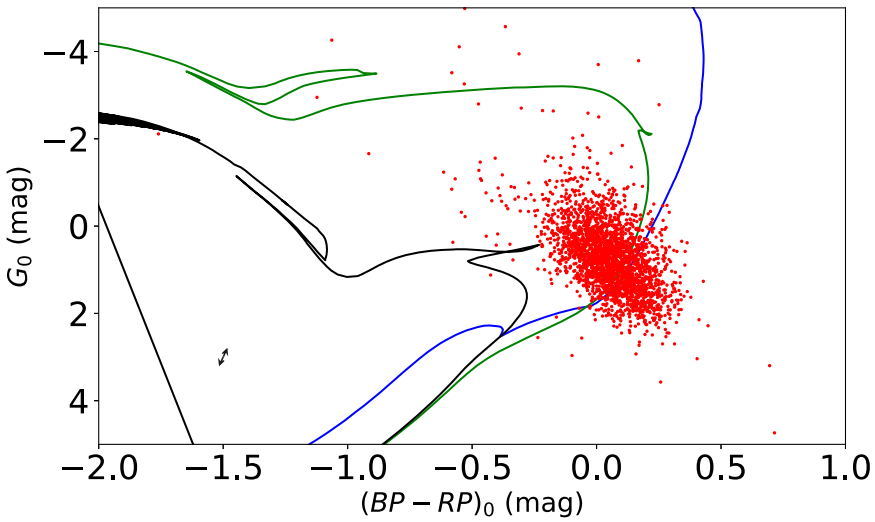

Figure 4. Distribution of Ap stars on the $(BP-RP)_0$ vs. G_0 diagram. The blue, green, and black lines denote isochrones calculated with ages of 10^7, 10^8, and 10^9 yr, respectively. The arrow shows the typical uncertainty of the position in this diagram.

The $(BP-RP)_0$ versus G diagram is presented in Figure 4. To estimate the typical uncertainty of the positions on this diagram, the median uncertainties of all parameters given by Gaia DR3 were taken as their typical uncertainties. The typical uncertainties of parallax, G, BP, and RP are 0.02 mas, 0.003 mag, 0.003 mag, and 0.004 mag, respectively. The typical uncertainty of the extinction in $(BP-RP)_0$ is similar to that in b–y, which is about 0.1 mag (Green et al. 2019). The arrow in Figure 4 indicates the typical uncertainty of the position on this diagram after considering reddening and parallax.

The mass values were determined through fitting isochrones provided by PARSEC (Bressan et al. 2012) on the $(BP-RP)_0$ versus G_0 diagram. Since most of the positions of stars overlap with both the main-sequence and pre-main-sequence stages, and no evolved stars are found, we assume that these stars are all in the main-sequence phase. Here we fit the mass values only for the stars whose positions have a distance of less than 0.05 mag to the theoretical grid point, since this is the *good fit* distance used in HPB2020. Under this criterion, the mass values of 1841 stars are derived. For the metallicity $[Z]$, we choose to use $[Z] = 0.02$ (Vagnozzi 2019), which has a good

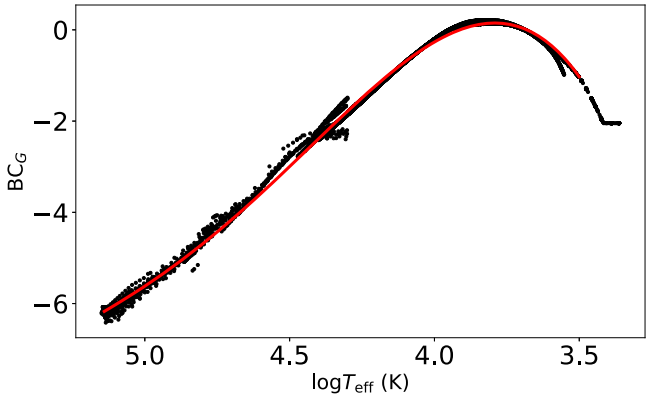

Figure 5. The relationship (red line) between BC_G and $T_{\rm eff}$, which is the fit curve of the data given by isochrones (black dots).

agreement with helioseismology rather than the latest solar abundance, $[Z] = 0.014$ (Asplund et al. 2021). This is reasonable because Ap stars are supposed to have higher metallicities since they are younger. The age range also follows that given in HPB2020 and is set to be 1 Myr–10 Gyr. Panel (c) in Figure 3 shows a histogram of the masses of our Ap stars. Most Ap stars have masses in the range of 2–3 $M_{\odot}$, which is the typical mass range of Ap stars.

The $\log g$ values were calculated based on a mass–luminosity relationship (Zhang & Zhao 2005), which comes from $L = 4\pi R^2 \sigma T^4$ and $g = GM/R^2$:

$$\log \frac{g}{g_{\odot}} = \log \frac{M}{M_{\odot}} + 4 \log \frac{T_{\rm eff}}{T_{\rm eff,\odot}} + 0.4(M_{\rm bol} - M_{\rm bol,\odot}), \quad (1)$$

where $M_{\rm bol} = G + BC_G$. The BC_G values were estimated from the effective temperatures. The isochrones give many sets of BC_G and $T_{\rm eff}$ values, and with them, the relationship between BC_G and $T_{\rm eff}$ is plotted and fitted in Figure 5. Since the spectral energy distribution of both hot stars and cool stars is more concentrated in the infrared and ultraviolet ranges, respectively, the bolometric correction is large and negative, which is consistent with the relationship shown in Figure 5. The BC_G values of our Ap stars are given based on the fitted relationship and the $T_{\rm eff}$ in Xiang et al. (2022).

Panel (d) in Figure 3 shows a histogram of the $\log g$ values of our Ap stars. The $\log g$ of these stars are in the range of main-sequence stars.

5.2. v*sin* i, *[Fe/H], [Si/H]*

The $T_{\rm eff}$, [Fe/H], [Si/H], and $v \sin i$ were extracted from the work of Xiang et al. (2022). [Fe/H]–$T_{\rm eff}$, [Si/H]–[Fe/H], and [Fe/H]–$v \sin i$ of our Ap stars were plotted and compared with those of about 452,000 stars in the catalog of Xiang et al. (2022). In Figure 6, the majority of our Ap stars exhibit high [Fe/H], and show high [Si/H] and low $v \sin i$, which are typical features of Bp and Ap stars and consistent with the inference made in Xiang et al. (2022).

In the left panel of Figure 6, [Fe/H] shows normal (abundance lower than 0.2 dex) to deficient Fe for cool Ap stars. This is consistent with the findings of Alecian (1996) and Hall (2020) and explains why our method tends to select hot stars. As shown in the middle panel, some stars appear to have normal [Fe/H] and [Si/H]. First, we check the errors of the [Si/H] measurements of these normal [Si/H] stars and compare them with those of other Ap stars in our catalog. As can be seen in the left panel of Figure 7, the distribution of the errors of these normal [Si/H] Ap stars tends to be larger. Moreover, as the Fe abundance in Ap stars goes from underabundant to overabundant as a function of increasing $T_{\rm eff}$, which is shown not only in this work but also in Alecian (1996) and Hall (2020), Si abundance may also be related with the $T_{\rm eff}$. The middle panel of Figure 7 shows that the normal [Si/H] stars contain a larger number of cooler stars ($T_{\rm eff} < 10{,}000$ K). Also, Ap stars are known to show a large range of abundance peculiarities, with some rare earth elements having nearly normal abundance, so in some cases, Si may not be overabundant. For example, Ghazaryan et al. (2019) pointed out that the Si abundances of some Ap stars can even be smaller than the solar abundance.

To verify this, we have checked how many libraries in MKCLASS can give a spectral classification with Si peculiarity for each star (see Section 3.2). The number of libraries that identify Si peculiarity is called the Si flag number. In Section 3.2, each star is classified by MKCLASS twice comparing with two different libraries. For one star, the Si flag number has three cases: if both of the two libraries identified Si peculiarity, then the Si flag number of this star is 2; if only one library identified Si peculiarity, then the Si flag number of this star is 1; and, if none identified Si peculiarity, then the Si flag number of this star is 0.

The right panel of Figure 7 shows the comparison of the Si flag number of normal Si Ap stars and other Ap stars in our catalog. Most of the Ap stars with an Si flag number less than 2 are normal Si Ap stars. Thus, a large error and low $T_{\rm eff}$ may result in an Ap star with normal [Si/H] and [Fe/H] so that there is no conspicuous Si peculiarity in this star.

Another problem is that some stars with high [Si/H] and [Fe/H] are not selected as Ap stars here. As mentioned before, our method has a bias toward Ap stars with depressions around 5200 Å.

5.3. *Evolutionary Stage from Gaia*

Gaia DR3 also provides evolution parameters, including mass, age, and evolution stage, from the Final Luminosity Age Mass Estimator (Creevey et al. 2022) by using the $T_{\rm eff}$, $\log g$, and [M/H] together with distance and magnitude as input parameters to derive luminosity and then comparing them with the BASTI (Hidalgo et al. 2018) solar metallicity stellar evolution models. Here we check the evolutionary stage distribution of these stars. In Figure 8, all of these stars fall in the range of the main-sequence stage, which is consistent with typical Ap stars and supports our earlier assumption given in Section 5.1.

6. Photometric Features

Our Ap stars were crossmatched with the target lists of TESS short cadence and Kepler observations. Forty-two stars (1.6% of the whole sample) only have TESS short cadence data while 25 stars (0.9%) only have Kepler data, and five stars (0.2%) have both. To search for rotation and pulsation features, a Fourier transform is applied for each star in both the low-frequency range (0–60 day^{-1}) and high-frequency range (60–300 day^{-1}). All the light curves and the periodograms are inspected by eye to double check them.

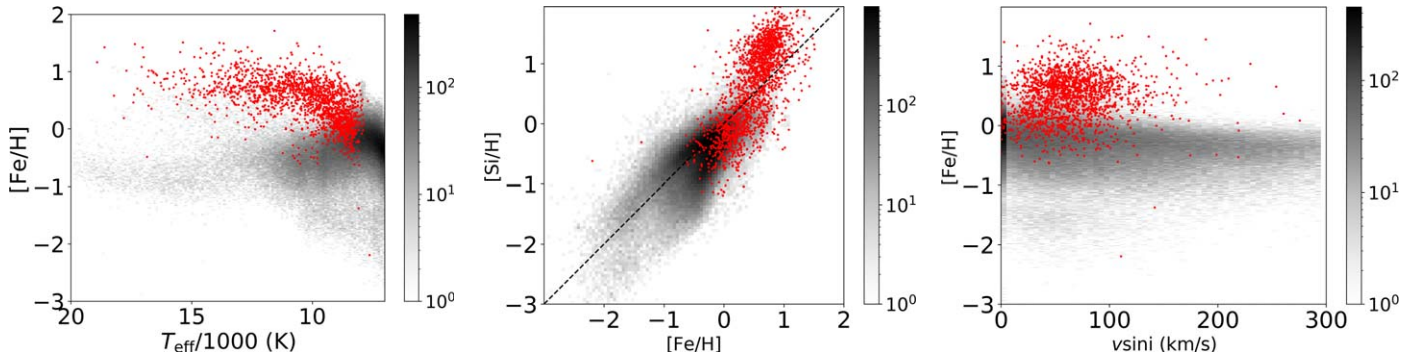

Figure 6. The distribution of our Ap stars (red dots) and the density distribution of the stars in Xiang et al. (2022) (gray dots) in the $T_{\rm eff}$–[Fe/H] (left), [Si/H]–[Fe/H] (middle), and $v \sin i$–[Fe/H] (right) planes.

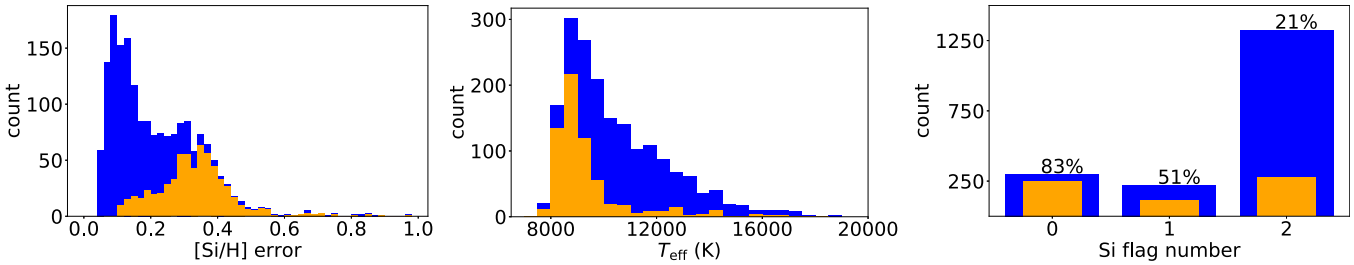

Figure 7. Histogram of [Si/H] errors (left panel), $T_{\rm eff}$ (middle panel), and Si flag number (right panel) of the normal [Si/H] stars in our catalog (orange) and all the Ap stars in our catalog (blue). The fractions of the normal [Si/H] stars among the Ap stars in each group are noted.

6.1. Rotation Features

Among these 72 stars, four stars (TIC 2934856, TIC 239801694, TIC 291258469, and TIC 434372218) do not show detectable rotation features. Mathys et al. (2020, 2022) found a total of 127 super slowly rotating Ap stars (ssrAp stars) that have long rotation periods so that no obvious rotational variability is seen in one TESS sector, or more. Among our four stars without rotation features detected, TIC 239801694 was identified as an ssrAp star candidate in Mathys et al. (2022), and the other three stars may also be candidates, or their rotation inclination angles are quite small.

Seven stars (TIC 22632159, TIC 34886401, TIC 238555975, TIC 292642288, TIC 293316714, TIC 239877980, and TIC 349510997) show clear rotation features but they are not included in any related literature. These are new rotational variable stars. Their periods and phase-folded light curves are shown in Figure 9. In addition, seven other stars (TIC 48354181, TIC 83096510, TIC 121603913, TIC 121732964, TIC 273130000, TIC 274024023, and TIC 416528957) have been identified as eclipsing binaries in the literature and they are noted in the catalog. The spectra of these seven binary stars are visually checked to make sure that they have Ap star peculiarities, such as enhancement of Si, Eu, and Sr. Although the binary systems mostly appear in Am stars whereas only about 20% of Ap stars are in binary systems (Abt & Snowden 1973), the possibility that these stars are Ap stars cannot be ruled out either.

6.2. Pulsation Features

For pulsation features, we find one roAp star candidate, TIC 21024812, one δ Scuti star candidate, TIC 119253179, and a known roAp star, TIC 272598185, whose roAp pulsation decreased and a new δ Scuti pulsation appeared. These stars will be discussed in the following subsections.

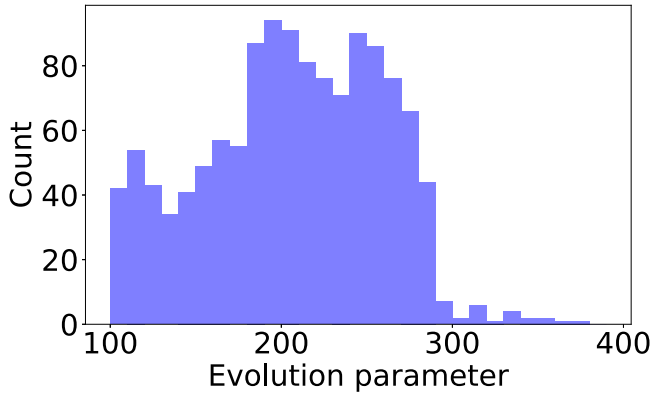

Figure 8. Distribution of the evolutionary stage of 1263 stars with evolution parameters. The x-axis is the evolution parameter, which for main-sequence stars ranges between 100 and 420.

6.2.1. The New roAp Star, TIC 21024812 (HD 14522)

TIC 21024812 was identified as an Ap star by Renson et al. (1991) with the spectral type of A2 SrEu. It has been discussed in several works (e.g., Joshi et al. 2006; Bernhard et al. 2020) that also searched for pulsations but no detection was reported. This star was observed in TESS Sector 18. A Fourier transform shows a significant low-frequency peak at 0.07174 day^{-1} (left panel in Figure 10). Taking the rotation frequency to be half of this, i.e., there is a double wave rotational variation, gives a rotation frequency of $\nu_{\rm rot} = 0.03587$ day^{-1} ($P_{\rm rot} = 27.88$ days), which is comparable to the rotation period given in Bernhard et al. (2020), $P_{\rm rot} = 26.36$ days. As the observation time span, 24 days, is shorter than the rotation period, and there are gaps in this sector of data, the pipeline processing may suppress some low frequencies; hence, one cannot get an accurate rotation period.

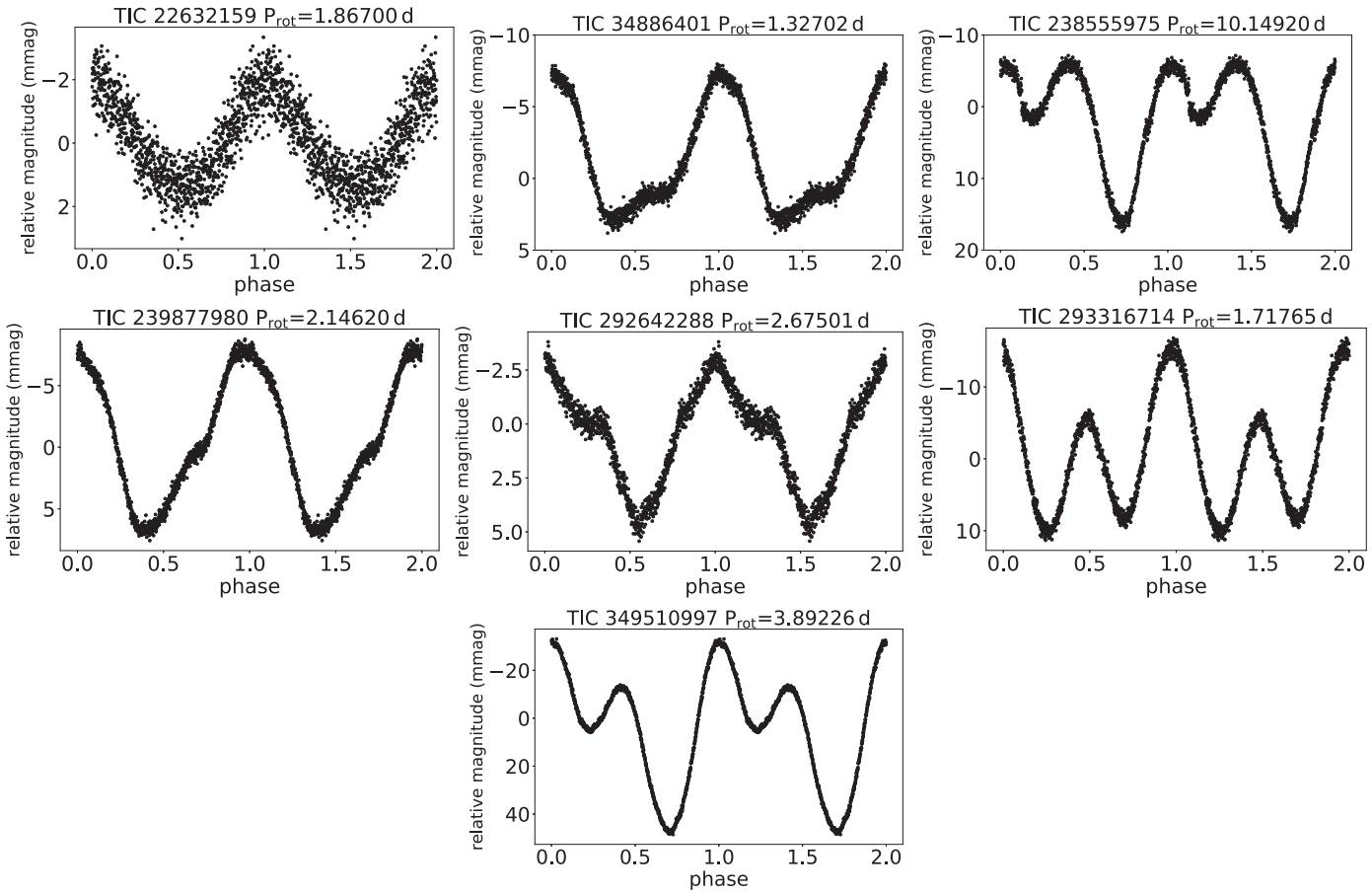

Figure 9. The phase-folded light curves of new rotational variable stars. The TIC IDs and periods are shown in each title.

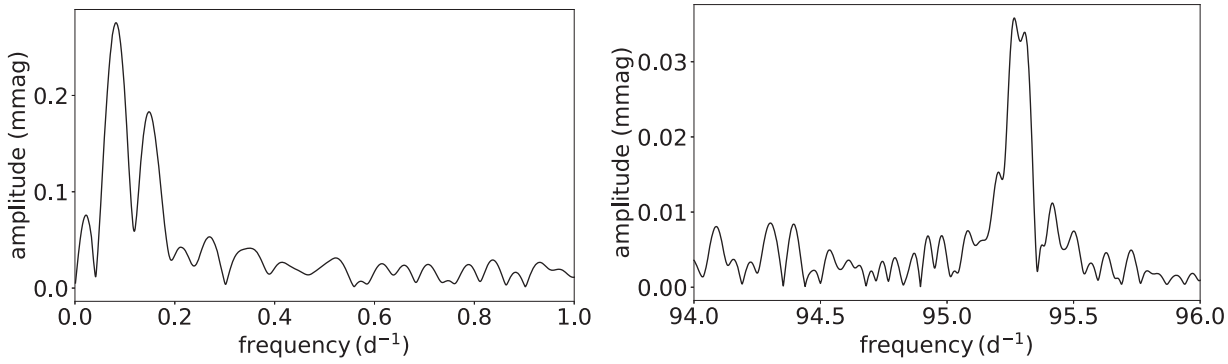

Figure 10. Periodogram of TIC 21024812 in the low- and high-frequency ranges.

After a Fourier transform in the high-frequency range, we have found a principal pulsation frequency at 95.264 day^{-1}, which is not fully resolved, as can be seen in Figure 10 (right panel). To get an optimized result of frequencies, linear and nonlinear least squares fits are used after removing rotation and other low-frequency signals. Since the gaps in TESS data make it difficult to determine the rotation period, we use the rotation period (P = 26.36 days) and the epoch (BJD = 2454059.3) given by Bernhard et al. (2020) to set the zero-point time to be t_0 = BJD 2458803.96, which is also near the middle time of the observed data. The results of the frequency analysis are listed in Table 2. A pre-whitening process leads to one side lobe being separated from the main frequency due to the rotation frequency, hence suggesting oblique pulsation. However, given the resolution limitation, this result is not robust. A longer time span of data is needed to confirm the rotation frequency.

Table 2
Nonlinear Least Squares Fit of the Frequency Multiplets for TIC 21024812

	Frequency (day^{-1})	Amplitude (mmag)	Phase (radians)
ν_1	95.263 ± 0.002	0.038 ± 0.003	2.37 ± 0.10
ν_2	95.311 ± 0.002	0.036 ± 0.003	1.65 ± 0.10

Note. The zero-point for the phases is t_0 = BJD 2458803.96.

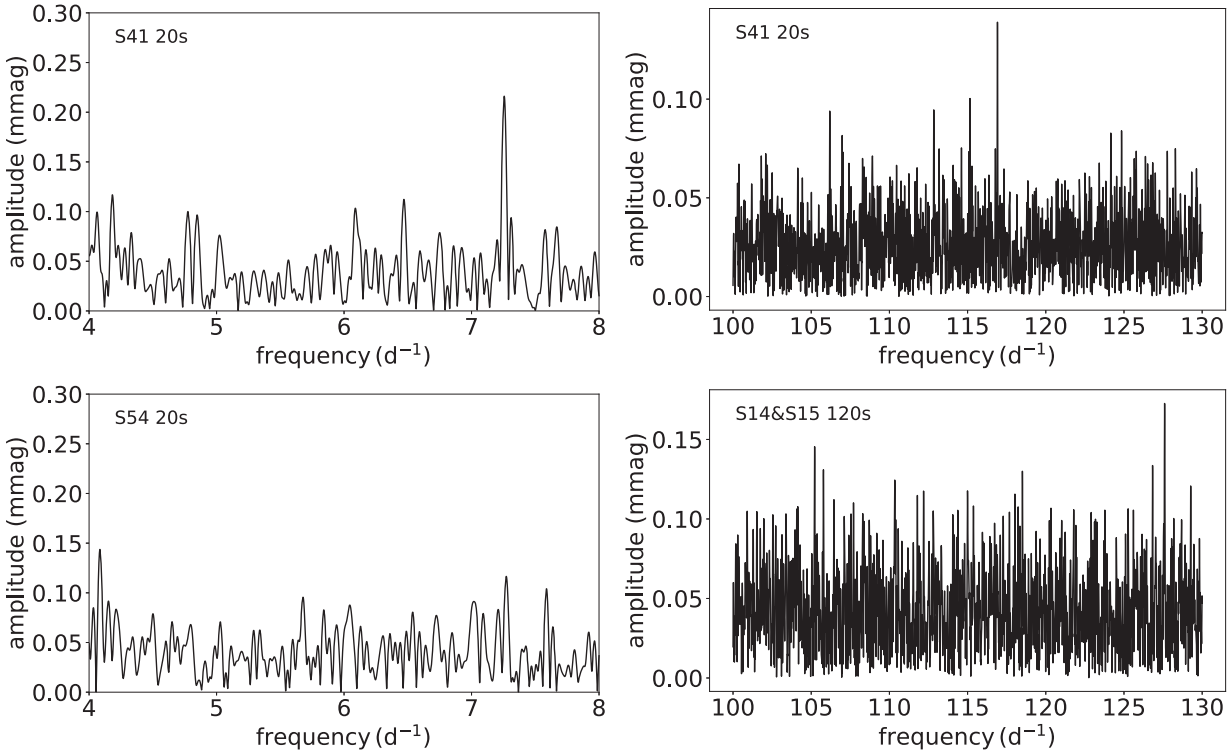

Figure 11. Periodogram of TIC 272598185 with data from TESS Sector 41 20 s cadence in the low- and high-frequency ranges (top two panels), TESS Sector 54 20 s cadence (left bottom), and TESS Sectors 14 and 15 120 s cadence (right bottom) zoomed in around 7.25 and 117 day^{-1} to show significant pulsation signals (top) or null results (bottom).

6.2.2. The New δ Scuti Pulsation of TIC 272598185 (KIC 10483436)

TIC 272598185 was identified as an roAp star with a frequency of around 117 day^{-1} by Balona et al. (2011) using Kepler short cadence data. Additionally, this star was observed 10 yr after Kepler's observations in TESS Sectors 14, 15, 41, and 54.

The roAp pulsation (right top panel of Figure 11) of around 117 day^{-1} is marginally detected in the Sector 41 20 s data with an amplitude just above 100 mmag, which is close to the noise level. But it falls lower than the high noise in the Sector 14 and 15 120 s data. The amplitude detected by TESS is above 0.1 mmag, which is significantly larger than the 0.07 mmag from Kepler. This may be caused by the slightly different passbands of the two missions, or by a change in amplitude in the 10 yr between the data sets.

A newly detected significant δ Scuti-type pulsation around 7.25 day^{-1} can be seen in the Sector 41 20 s data (Figure 11, left top panel), but not the Sector 54 data (Figure 11, left bottom panel). The presence of the low-amplitude δ Sct mode suggests a probable magnetic field strength of less than a few kilogauss (Murphy et al. 2020).

7. Conclusions

We have found 2700 Ap stars by searching LAMOST DR9 for the 5200 Å flux depression, with all of the spectra having been inspected by eye. A detailed spectral classification of our Ap stars is given by applying a modified MKCLASS program developed by HPB2020.

Our Ap star catalog is compared with other related catalogs. Since each catalog searched for CP stars using different methods, the stars identified as Ap star candidates may have different selection biases leading to few stars in common among these catalogs.

Statistical analyses of the stellar parameters $T_{\rm eff}$, $\log g$, absolute magnitude, mass, and evolutionary status are carried out. We find that most stars have $T_{\rm eff}$ and $\log g$ typical of main-sequence stars with masses in the range of 2–3 $M_{\odot}$. These properties are in agreement with those of previously known Ap stars. From the evolution parameters given by Gaia DR3, all the stars are in the main sequence.

The metallicities, [Si/H] and [Fe/H], together with $v \sin i$ of our Ap stars are compared with those of non-peculiar stars. A lower $v \sin i$, higher Fe abundance, and much higher Si abundance of our Ap stars can be clearly seen.

After crossmatching our Ap star catalog with the target lists of TESS and Kepler data, we inspect the rotation and pulsation features of 72 stars in common. Among these Ap stars, seven stars are new rotational variable stars and three do not show rotation features; hence, they may be super slowly rotating Ap star candidates. We also find a new roAp star, TIC 21024812. For a known roAp star, TIC 272598185, we find a new δ Scuti pulsation that appeared.

Our Ap star catalog is complementary to other existing Ap star catalogs, and the method used to search for Ap star candidates was shown to be valid. Our catalog is hopefully valuable for the further study of Ap stars. In the future, by measuring the magnetic fields and obtaining high-resolution spectroscopic observations of the Ap stars in our catalog, the

effect of the magnetic field on the abundance and rotation can be studied. Combined with the photometric data, these stars are also good candidates for searching for roAp stars and ssrAp stars.

This work was funded by the National Natural Science Foundation of China (NSFC grant Nos. 11973001, 12090040, 12090044, U1731108, and 11833002) and the National Key R&D Program of China (No. 2019YFA0405500).

This work has made use of data products from the Guo Shou Jing Telescope LAMOST. LAMOST is a National Major Scientific Project built by the Chinese Academy of Sciences. Funding for the project has been provided by the National Development and Reform Commission. LAMOST is operated and managed by the National Astronomical Observatories, Chinese Academy of Sciences.

We used data from the European Space Agency mission Gaia (http://www.cosmos.esa.int/Gaia), processed by the Gaia Data Processing and Analysis Consortium (DPAC; see http://www.cosmos.esa.int/web/Gaia/dpac/consortium).

Some of the data presented in this paper were obtained from the Mikulski Archive for Space Telescopes (MAST) at the Space Telescope Science Institute. The specific observations analyzed can be accessed via doi:10.17909/j98f-cs20.

Appendix

Table A1 is an extract of the Ap star catalog in this work.

Table A1
Example of Our Ap Star Catalog

ObsID	R.A. (deg)	Decl. (deg)	G_0 (mag)	$(BP-RP)_0$ (mag)	a (mag)	Distance (pc)	spt-liblamost	spt-libnor36	Note	Gaia id
2416019	29.31	59.79	0.52	0.12	0.58	1721.97	kB9.5hA2mA4 bl4077bl4130Si3856Si5041Si5056	A0 II-III bl4077bl4130Si3856Si5041Si5056		507868307825704320
4116106	46.79	53.86	−0.09	0.02	0.58	679.40	B8 III (bl4077)bl4130Si3856Si5056Cr4172	B8 III-IV bl4130Si3856Si5041Si5056Cr4172		447095826254298112
8312154	52.41	6.09	1.13	−0.04	0.59	873.41	B9 IV-V bl4077bl4130Si3856Si5041Si5056Cr4172	B9 IV-V bl4077bl4130Si3856Si5041Si5056Cr4172		3276185836320362624
15005220	55.73	48.90	0.67	0.08	0.59	2583.10	B9 II (bl4077)bl4130Si5056Cr4172	A0 II (bl4077)bl4130Si5041Si5056		248775986236536576
15010139	53.09	50.21	−0.15	0.08	0.59	3099.77	B8 III bl4077bl4130Si5041Si5056Cr4172	A0 II-III bl4077bl4130Si5041Si5056Cr4172		441988560381708160
15016079	54.63	51.57	−0.85	0.11	0.58	1920.18	B8 III-IV (bl4077)bl4130Si3856Cr4172	B9.5 III (bl4077)bl4130Si3856Si5056Cr4172		442169631902357248
15016105	55.70	51.98	1.26	0.08	0.60	1275.35	B8 IV bl4077bl4130Si3856Si5041Si5056Cr4172	B9 III-IV bl4077bl4130Si3856Si5041Si5056Cr4172		443661948360036352
15301125	34.22	56.52	0.28	−0.00	0.57	3638.02	B8 IV bl4130Si3856Si5041Si5056	B9 III bl4130Si3856Si5041Si5056		458330395554092160
15303061	31.11	58.59	0.05	−0.02	0.59	3633.01	B9 II-III bl4130Si3856Si5041Si5056Cr4172	B9.5 III (bl4130)Si3856Si5041Si5056		506958083995671424
15303088	31.09	58.35	1.54	0.12	0.58	1878.73	A0 II-III bl4130Si3856Eu4205Cr4172	B9.5 III-IV (bl4077)bl4130Si3856Si5056Eu4205Cr4172		506942312875851264
15304172	32.93	58.53	1.54	0.09	0.59	2048.16	B9 IV-V bl4077bl4130Si3856Si5041Si5056Cr4172	B9.5 IV-V bl4077bl4130Si3856Si5041Si5056Cr4172		506818927055051776
107803140	87.98	20.49	0.70	−0.09	0.56	953.54	B8 IV Eu4205Cr4172	B8 IV-V Si5056Eu4205		3399810865002711424
107806193	90.39	19.58	1.17	−0.00	0.57	713.63	A0 IV-V Si5056Cr4172	A0 IV-V Si5041Si5056Cr4172		3374701322257770368
107814144	86.72	21.08	0.25	0.14	0.58	1746.30	B8 II-III (bl4077)bl4130	B9.5 II-III (bl4077)bl4130Si5041Si5056		3400054338109166080
107904250	89.14	20.35	1.08	0.04	0.58	1120.49	B9 IV bl4077bl4130Eu4205Cr4172Sr4216	B9.5 IV bl4077bl4130Eu4205Cr4172Sr4216		3423035715975909888
107905154	88.38	19.62	−0.26	0.18	0.58	2109.28	B8 IV bl4077bl4130Si3856Cr4172Sr4216	B9 IV-V bl4077bl4130Si3856Si5041Cr4172Sr4216		3398874703869380736
165907022	301.37	44.12	0.17	−0.02	0.58	1613.04	A1 IV-V bl4077bl4130Eu4205Cr4172	A1 IV-V bl4077bl4130Eu4205Cr4172		2081867542833415168
166108162	66.57	33.22	0.23	0.01	0.58	1160.96	B9 III bl4077bl4130Si3856Si5041Si5056Eu4205Cr4172	B8 IV-V bl4077bl4130Si3856Si5041Si5056Eu4205Cr4172	new rotation	172534338135032576
166115176	65.94	35.13	1.80	0.25	0.58	338.80	kA2hA3mA6 bl4077bl4130Eu4205Cr4172Sr4216	kA2hA5mA8 bl4077bl4130Si5041Eu4205Cr4172Sr4216		176314665270306944
167502103	78.34	39.00	0.77	−0.05	0.58	1031.67	B8 IV-V bl4077bl4130Si3856Cr4172	B8 IV-V bl4077bl4130Si3856Cr4172		188235776501129600
204805179	93.29	34.40	0.99	0.07	0.59	1000.69	B8 III-IV bl4077bl4130Si3856Si5041Si5056Cr4172	B8 IV-V (bl4077)bl4130Si3856Si5041Si5056Cr4172	new rotation	3452249426397874816
204815021	94.29	36.38	−0.13	-0.19	0.57	1584.86	B4 II-III (bl4130)	B4 III-IV Si5041		3453051764937380096
204815135	94.81	36.39	0.02	−0.07	0.59	1418.80	B8 II-III bl4077bl4130Si5041Si5056Cr4172	B8 IV-V bl4077bl4130Si5041Si5056Cr4172		3453040838540792960
204905041	93.96	34.16	0.47	0.05	0.57	3217.13	B9 II-III bl4077bl4130Si5041Si5056	B9.5 II-III bl4077bl4130Si3856Si5041Si5056		3452198269036345984
204908180	94.89	34.14	0.64	0.06	0.58	1071.08	A0 IV-V bl4077(bl4130)Eu4205Cr4172	A0 IV bl4077bl4130Cr4172		3440503068792793472
238012135	283.69	48.34	1.52	0.08	0.58	1653.30	kA1hA3mA4 bl4077bl4130Si3856Eu4205Cr4172Sr4216	A1 V bl4077bl4130Si3856Eu4205Cr4172Sr4216	EB	2131718510982169728
240511113	260.92	15.59	0.98	0.23	0.58	635.77	kA4hA8mA8 bl4077bl4130Si3856Si5056Sr4216	A9 V bl4077bl4130Si3856Si5056Sr4216		4543881060489030528
240515196	260.15	14.39	0.63	−0.08	0.56	1305.56	B9.5 IV Si5056	B9.5 IV-V (bl4130)Si5041Si5056		4543145182269101312
243011020	285.39	41.87	1.60	0.09	0.58	310.99	A1 IV-V bl4077bl4130Si3856Si5041Eu4205Cr4172Sr4216	A1 IV-V bl4077bl4130Si3856Si5041Eu4205Cr4172Sr4216		2104073451467807232
243113025	288.63	40.45	0.94	0.04	0.59	371.96	B9 V bl4077bl4130Si3856Eu4205Cr4172	B9 V bl4077bl4130Si3856Eu4205Cr4172	EB	2101314128259814912
243113207	288.36	40.17	0.39	−0.01	0.59	3937.68	B9 V bl4077bl4130Cr4172	B9 IV-V bl4077bl4130Cr4172	EB	2101303373661496704
297006249	87.21	35.04	0.66	−0.08	0.58	644.47	B9 V bl4077bl4130Si3856Eu4205Cr4172	B9 V bl4077bl4130Si3856Cr4172		3454789508706967296
297007224	87.08	33.59	1.26	0.02	0.58	514.48	kA4hA9mA8 bl4077bl4130Si3856Si5041Si5056Eu4205Cr4172Sr4216	kA4hA9mF1 bl4077bl4130Si3856Si5041Si5056Eu4205Cr4172Sr4216	no rotation	3454347367594873088
297007241	86.65	33.32	−0.38	0.10	0.57	2402.48	B8 II-III (bl4077)bl4130Si3856Si5056	B8 IV (bl4077)bl4130Si3856Si5056		3448344068466322048
297008011	86.43	35.05	1.39	−0.03	0.59	884.34	A0 IV bl4077bl4130Si3856Cr4172Sr4216	A0 III-IV bl4077bl4130Si3856Si5056Cr4172Sr4216		3455528960339050240
297008020	86.39	35.05	1.51	0.08	0.59	909.82	A0 IV-V bl4077bl4130Si3856Eu4205Cr4172	A0 IV bl4077bl4130Si3856Si5041Cr4172		3455438113192188544
297010019	83.13	35.45	1.24	0.04	0.59	1955.14	B9 II-III bl4077bl4130Si3856Si5041Si5056Cr4172	B8 IV bl4077bl4130Si3856Si5041Si5056Cr4172		183081609586291712
297010107	83.03	35.28	0.65	−0.09	0.58	1018.56	B8 III-IV bl4077bl4130Si3856Si5041Si5056Cr4172	B8 IV-V bl4077bl4130Si3856Si5041Si5056Cr4172		183077830015921408
297010223	83.79	35.10	0.80	0.03	0.58	1249.87	B8 IV-V (bl4077)bl4130Si3856Cr4172	B9 IV-V (bl4077)bl4130Si3856Cr4172		183101911891717376
733507176	98.64	19.11	0.44	0.03	0.59	2362.68	B8 II-III bl4077bl4130Si3856Si5041Si5056	B9 III bl4077bl4130Si3856Si5041Si5056		3371482669469578752
733508216	97.65	19.26	2.58	0.25	0.60	1318.25	A0 III bl4130Si3856Eu4205Cr4172	B9 V bl4130Si3856Cr4172		3372241852186145792
733510195	94.84	19.36	0.29	0.20	0.59	2655.07	B8 III (bl4130)Si3856Si5056Cr4172	B8 IV bl4130Si3856Si5041Si5056Cr4172		3373932454393421824
733511065	97.26	22.30	0.45	0.13	0.58	2624.63	B8 III-IV bl4077bl4130Si3856Si5041Si5056Cr4172	B9 III bl4077bl4130Si3856Si5041Si5056		3376444421848798976
733514197	94.86	20.69	0.58	−0.01	0.59	1240.20	B8 III-IV bl4077Si3856Si5041Si5056Cr4172	B8 V bl4077Si3856Si5056Cr4172		3375810901289300608
733515133	97.14	21.58	0.23	0.00	0.58	1134.72	B9 III-IV (bl4130)Eu4205Cr4172	B9 IV (bl4130)Cr4172		3376120482532172288

Note. The full catalog is available electronically.

(This table is available in its entirety in machine-readable form.)

ORCID iDs

Fangfei Shi https://orcid.org/0000-0003-2399-8216
Huawei Zhang https://orcid.org/0000-0002-7727-1699
Jianning Fu https://orcid.org/0000-0001-8241-1740
Donald Kurtz https://orcid.org/0000-0002-1015-3268

References

Abt, H. A., & Snowden, M. S. 1973, ApJS, 25, 137
Alecian, G. 1996, A&A, 310, 872
Andrae, R., Fouesneau, M., Sordo, R., et al. 2022, arXiv:2206.06138
Asplund, M., Amarsi, A. M., & Grevesse, N. 2021, A&A, 653, A141
Babusiaux, C., Fabricius, C., Khanna, S., et al. 2022, arXiv:2206.05989
Bailer-Jones, C. A. L., Rybizki, J., Fouesneau, M., Demleitner, M., & Andrae, R. 2021, AJ, 161, 147
Balona, L. A., Cunha, M. S., Gruberbauer, M., et al. 2011, MNRAS, 413, 2651
Bernhard, K., Hümmerich, S., & Paunzen, E. 2020, MNRAS, 493, 3293
Bidelman, W. P. 1956, VA, 2, 1428
Bidelman, W. P., & Keenan, P. C. 1951, ApJ, 114, 473
Bressan, A., Marigo, P., Girardi, L., et al. 2012, MNRAS, 427, 127
Chojnowski, S. D., Hubrig, S., Hasselquist, S., et al. 2019, ApJL, 873, L5
Creevey, O. L., Sordo, R., Pailler, F., et al. 2022, arXiv:2206.05864
Cui, X.-Q., Zhao, Y.-H., Chu, Y.-Q., et al. 2012, RAA, 12, 1197
Gaia Collaboration, Prusti, T., de Bruijne, J. H. J., et al. 2016, A&A, 595, A1
Ghazaryan, S., & Alecian, G. 2016, MNRAS, 460, 1912
Ghazaryan, S., Alecian, G., & Hakobyan, A. A. 2019, MNRAS, 487, 5922
Gray, R. O., & Corbally, C. J. 2014, AJ, 147, 80
Gray, R. O., Corbally, C. J., Cat, P. D., et al. 2016, AJ, 151, 13
Green, G. M., Schlafly, E., Zucker, C., Speagle, J. S., & Finkbeiner, D. 2019, ApJ, 887, 93
Hall, M. 2020, PhD thesis, Univ. of Central Lancaster, http://clok.uclan.ac.uk/34655/
Hidalgo, S. L., Pietrinferni, A., Cassisi, S., et al. 2018, ApJ, 856, 125
Hümmerich, S., Mikulášek, Z., Paunzen, E., et al. 2018, A&A, 619, A98
Hümmerich, S., Paunzen, E., Bernhard, K., et al. 2020, A&A, 640, A40
Joshi, S., Mary, D. L., Martinez, P., et al. 2006, A&A, 455, 303
Khan, S. A., & Shulyak, D. V. 2007, A&A, 469, 1083
Kodaira, K. 1969, ApJL, 157, L59
Kupka, F., Paunzen, E., & Maitzen, H. M. 2003, MNRAS, 341, 849
Maitzen, H. M. 1976, A&A, 51, 223
Maitzen, H. M., Paunzen, E., & Netopil, M. 2018, CoSka, 48, 218
Maitzen, H. M., Pressberger, R., & Paunzen, E. 1998, A&AS, 128, 573
Majewski, S. R., Schiavon, R. P., Frinchaboy, P. M., et al. 2017, AJ, 154, 94
Mamajek, E. 2022, A Modern Mean Dwarf Stellar Color and Effective Temperature Sequence, version 2022.04.16, http://www.pas.rochester.edu/~emamajek/EEM_dwarf_UBVIJHK_colors_Teff.txt
Mathys, G. 2017, A&A, 601, A14
Mathys, G., Kurtz, D. W., & Holdsworth, D. L. 2020, A&A, 639, A31
Mathys, G., Kurtz, D. W., & Holdsworth, D. L. 2022, A&A, 660, A70
Michaud, G. 1970, ApJ, 160, 641
Murphy, S. J., & Paunzen, E. 2017, MNRAS, 466, 546
Murphy, S. J., Saio, H., Takada-Hidai, M., et al. 2020, MNRAS, 498, 4272
Preston, G. W. 1974, ARA&A, 12, 257
Qin, L., Luo, A.-L., Hou, W., et al. 2019, ApJS, 242, 13
Recio-Blanco, A., de Laverny, P., Palicio, P. A., et al. 2022, arXiv:2206.05541
Renson, P., Gerbaldi, M., & Catalano, F. A. 1991, A&AS, 89, 429
Renson, P., & Manfroid, J. 2009, A&A, 498, 961
Scholz, R. -D., Chojnowski, S. D., & Hubrig, S. 2019, A&A, 628, A81
Shore, S. N., & Adelman, S. J. 1974, ApJ, 191, 165
Stigler, C., Maitzen, H. M., Paunzen, E., & Netopil, M. 2014, A&A, 562, A65
Vagnozzi, S. 2019, Atoms, 7, 41
Xiang, M., Rix, H.-W., Ting, Y.-S., et al. 2022, A&A, 662, A66
Zhang, H. W., & Zhao, G. 2005, MNRAS, 364, 712
Zhao, G., Zhao, Y.-H., Chu, Y.-Q., Jing, Y.-P., & Deng, L.-C. 2012, RAA, 12, 723